

Original citation:

Du, Dongwei, Lan, Rong, Humphreys, John, Xu, Wei, Xie, Kui, Wang, Huanting and Tao, Shanwen. (2017) Synthesis of NiMoS₄ for high-performance hybrid supercapacitors. Journal of The Electrochemical Society, 164 (12). A2881-A2888.

Permanent WRAP URL:

<http://wrap.warwick.ac.uk/93990>

Copyright and reuse:

The Warwick Research Archive Portal (WRAP) makes this work by researchers of the University of Warwick available open access under the following conditions. Copyright © and all moral rights to the version of the paper presented here belong to the individual author(s) and/or other copyright owners. To the extent reasonable and practicable the material made available in WRAP has been checked for eligibility before being made available.

Copies of full items can be used for personal research or study, educational, or not-for-profit purposes without prior permission or charge. Provided that the authors, title and full bibliographic details are credited, a hyperlink and/or URL is given for the original metadata page and the content is not changed in any way.

Publisher's statement:

<http://dx.doi.org/10.1149/2.0071713jes>

A note on versions:

The version presented here may differ from the published version or, version of record, if you wish to cite this item you are advised to consult the publisher's version. Please see the 'permanent WRAP URL' above for details on accessing the published version and note that access may require a subscription.

For more information, please contact the WRAP Team at: wrap@warwick.ac.uk

Synthesis of NiMoS₄ for high-performance hybrid supercapacitors

Dongwei Du,^a Rong Lan,^a John Humphreys,^a Wei Xu,^a Kui Xie,^c Huanting Wang,^b and
Shanwen Tao,^{a,b,z}

^a School of Engineering, University of Warwick, Coventry CV4 7AL, UK

^b Department of Chemical Engineering, Monash University, Clayton, Victoria 3800, Australia

^c Key Lab of Design and Assembly of Functional Nanostructure, Fujian Institute of Research on the Structure of Matter, Chinese Academy of Sciences, Fuzhou, Fujian 350002, China

^z Corresponding author: Shanwen Tao

E-mail: S.Tao.1@warwick.ac.uk

Tel: +44 (0) 24 761 51680

Fax: +44 (0) 24 76 418922

Abstract

Transition metal sulfides have been suggested as promising materials for efficient energy storage with superior electrochemical performances. Compound NiMoS₄-A was synthesized by a facile chemical co-precipitation process, followed by calcining at 450 °C in Ar. The as-prepared NiMoS₄-A electrode exhibits a high specific capacity of 313 C g⁻¹ at 1 A g⁻¹ and good rate capability (83% retention at 10 A g⁻¹). Electrochemical impedance spectroscopy (EIS) results indicate that the good performances could be attributed to the low internal and charge transfer resistances. Additionally, the quantitative charge storage analysis reveals that the Faradaic redox process dominates at lower scan rates (78% at 1 mV s⁻¹), while the capacitive effect dominates at higher scan rates (56% at 20 mV s⁻¹). Furthermore, a hybrid supercapacitor (HSC), with NiMoS₄-A as the positive electrode and activated carbon (AC) as the negative electrode, displays a high energy density of 35 Wh kg⁻¹ at an average power density of 400 W kg⁻¹. Meanwhile, the HSC exhibits excellent cycle stability, maintaining 82% of the initial capacitance after 10000 charge-discharge cycles even at a high current density of 5 A g⁻¹. These good electrochemical performances indicate that NiMoS₄-A is a promising positive electrode material for hybrid supercapacitors.

1. Introduction

The demand for high-performance electrochemical energy storage devices is ever-growing as they are critical components for portable electronics, electric vehicles, and an efficient storage medium for energy from renewable sources.¹ Rechargeable batteries are considered as a promising technology which can meet these requirements.^{2, 3} However, batteries often offer low charge/discharge rate and power density which is insufficient when a short-burst of peak power is needed.⁴ To solve this problem, researchers have shown a tremendous amount of interest on electrochemical supercapacitors owing to their high powder density, rapid charge-discharge rate and outstanding cycle life.⁵⁻⁷ According to the charge storage mechanisms, the supercapacitor can be classified into two types: electrical double-layer capacitors (EDLCs) and pseudocapacitors.⁸ EDLCs store charges via reversible adsorption/desorption of cations and anions at the electrode/electrolyte interface while pseudocapacitors store charges through fast Faradic reactions at the electrode surface.⁹ Currently, most commercial supercapacitors are EDLCs which possess better performance in terms of cycle life and power density, but the low specific capacitance and energy density limit their widespread applications.¹⁰ On the basis of these circumstances, it is supposed that developing hybrid supercapacitors (HSCs) could be a promising approach to fulfill the high energy density without sacrificing the power density and cycle life.¹¹ HSCs are usually composed of one battery-type electrode and one capacitive electrode, which could combine advantages of batteries and supercapacitors, delivering enhanced capacitance and high energy density.^{1, 8}

Transition metal oxides are the most common battery or pseudocapacitive materials and have been extensively studied due to their high theoretical capacities and low cost.⁷ Many materials have been claimed holding good supercapacitor performances such as MnO_2 ,^{12, 13} NiO ,^{14, 15} MoO_3 ^{16, 17} etc. However, the performances of metal oxides often suffer from poor conductivity and mechanical stability especially under high rates.¹⁸ It is known that the metal

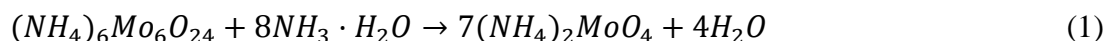
sulfides usually possess higher conductivity than the corresponding oxides. Therefore, plenty of sulfides have been applied as new pseudocapacitive materials with good performances being obtained. For instance, Pang *et al.* prepared a NiS₂ nanocube electrode via a microwave-assisted method, demonstrating a large specific capacitance of 695 F g⁻¹ at 1.25 A g⁻¹ and an excellent cycling performance with 93.4% retention after 3000 cycles.¹⁹ Acerce *et al.*'s research indicates that chemically exfoliated nanosheets of MoS₂ can efficiently intercalate H⁺, Li⁺, Na⁺ and K⁺ ions to achieve high capacitance in a variety of aqueous electrolytes.²⁰ As NiMoO₄ has been confirmed as a good capacitive material,^{21, 22} it can be deduced that, its sulfide analogue, NiMoS₄ would also be a good candidate for supercapacitors. NiMoS₄ has been applied in hydrogen evolution²³ and dye-sensitized solar cells²⁴ as previously reported.

Herein, we report a ternary compound NiMoS₄-A which was synthesized by a facile chemical co-precipitation process followed by calcining at 450 °C in Ar. Physical and electrochemical properties of the NiMoS₄-A were extensively studied. The NiMoS₄-A electrode exhibits a high specific capacity of 313 C g⁻¹ at 1 A g⁻¹ and a good rate capability (83% retention at 10 A g⁻¹). Electrochemical impedance spectroscopy (EIS) results indicate that the good performances could be attributed to the low internal and charge transfer resistances. Moreover, a hybrid supercapacitor (HSC), with NiMoS₄-A as the positive electrode and activated carbon (AC) as the negative electrode, was fabricated to investigate the performances in practical energy storage devices. The HSC displays a high energy density of 35 Wh kg⁻¹ at an average power density of 400 W kg⁻¹. Meanwhile, an excellent cycle stability is achieved: 82% of the initial capacitance is retained after 10000 charge-discharge cycles even at a high current density of 5 A g⁻¹. These results indicate that NiMoS₄-A is a promising electrode material for high energy storage devices.

2. Experimental

2.1. Synthesis of (NH₄)₂MoS₄

(NH₄)₂MoS₄ was synthesized following a previously reported method.²³ To prepare the (NH₄)₂MoS₄, 7.5 g (NH₄)₆Mo₇O₂₄·4H₂O was dissolved in 5 mL ammonia and 10 mL H₂O under constant stirring. Then 60 mL of 20% (NH₄)₂S solution was added dropwise at room temperature. The system was kept in a water bath at 60 °C for 2 h. After that, the obtained red-brown solution was cooled in an ice-bath to allow the (NH₄)₂MoS₄ to crystallize. Finally, the resultant crystals were collected by centrifugation and washed with ethanol several times. The products were dried under vacuum at 30 °C. The mechanism of formation of the (NH₄)₂MoS₄ crystal can be expressed in the equations:²⁵



2.2. Synthesis of NiMoS₄

Firstly, 4 mmol (NH₄)₂MoS₄ was dispersed in 30 mL water with 5 mL ethanol. Similarly, 4 mmol Ni(NO₃)₂·6H₂O was dissolved in 30 mL water with 5 mL ethanol. The Ni(NO₃)₂ solution was added into the (NH₄)₂MoS₄ solution under vigorous magnetic stirring and kept overnight. The black precipitate was collected by centrifugation, washed with distilled water and absolute ethanol several times, and finally vacuum dried at 30 °C. In addition, the NiMoS₄ was further calcined at 450 °C for 2 h under Ar atmosphere. For comparison, the calcined NiMoS₄ was denoted as NiMoS₄-A.

2.3. Material Characterizations

Physical Characterization

X-ray Diffraction (XRD) patterns were obtained on a Panalytical X'Pert Pro Multi-Purpose Diffractometer (MPD) with Cu K α 1 radiation working at 45 kV and 40 mA. The morphologies and microstructures of the as-synthesized materials were identified using scanning electron microscopy (SEM) (ZEISS SUPRA 55-VP). The elemental compositions were investigated by Energy-dispersive X-ray spectroscopy studies (EDX) attached to the SEM.

Electrochemical measurements

The working electrode was prepared as follows: an homogeneous slurry comprised of the active materials, acetylene black and polytetrafluoroethylene (PTFE) in a mass ratio of 8 : 1 : 1 was coated onto Ni foam ($1 \times 1 \text{ cm}^2$), pressed at 10 MPa, and finally dried at 60 °C under vacuum. The mass loading of the active materials on each working electrode was 1-2 mg cm⁻². The performance of the prepared working electrode was firstly investigated in a three-electrode system with a piece of Pt mesh ($1 \times 1 \text{ cm}^2$) and an Ag/AgCl electrode (sat. KCl) serving as counter and reference electrodes, respectively. Hybrid supercapacitors were also fabricated using the as-prepared working electrode as the positive electrode and an activated carbon (AC) electrode as the negative electrode. The electrochemical measurements including cyclic voltammetry (CV), galvanostatic charge–discharge (GCD) and electrochemical impedance spectroscopy (EIS) were carried out on a Solartron 1470E/1455 multichannel cell test system. Impedance spectroscopy were recorded with a potential amplitude of 5 mV at open circuit potential. All the measurements were performed at room temperature in 2 M KOH aqueous solution as electrolyte.

2.4. Calculations

The specific capacity of the electrode can be calculated from CV curves by the equation:^{26,}

27

$$C_p = \frac{1}{2mv} \int I(V)dV \quad (3)$$

where C_p is the specific capacity ($C\ g^{-1}$), m is the mass the active materials (g), v is the scan rate ($V\ s^{-1}$), I is the current at V (A) and dV is the differential potential.

The specific capacity could also be determined from the galvanostatic charge-discharge curves according to the following equation:^{28, 29}

$$C_p = \frac{I \times \Delta t}{m} \quad (4)$$

where C_p is the specific capacity ($C\ g^{-1}$), I is the constant discharge current (A), Δt is the discharge time (s), m is the mass the active materials (g).

In order to achieve high electrochemical performance of the hybrid supercapacitor (HSC), the mass ratio between the positive and negative electrodes was optimized by balancing the charge stored at the electrodes. The charge stored by electrode can be obtained by the equation:^{26, 30}

$$q = C_p \times m \quad (5)$$

where C_p is the specific capacity ($C\ g^{-1}$), m is the mass of the active materials (g). According to equation (5) and $q_+ = q_-$, the mass ratio of active materials on the positive and negative electrode in a hybrid supercapacitor can be calculated:³¹

$$\frac{m_+}{m_-} = \frac{C_-}{C_+} \quad (6)$$

Since the HSC performed quasi rectangular CV curves, the specific capacitance could be calculated as:^{28, 29}

$$C_s = \frac{I \times \Delta t}{m \times \Delta V} \quad (7)$$

where C_s is the specific capacitance ($F\ g^{-1}$), I is the constant discharge current (A), Δt is the discharge time (s), m is the total mass of the active materials on both the positive and negative electrode (g), and ΔV is the potential change excluding the IR drop in the discharge step (V).

The energy densities and corresponding power densities of the HSC were obtained from the following equations:^{22, 32}

$$E = \frac{C_s V^2}{2 \times 3.6} \quad (8)$$

$$P = \frac{E \times 3600}{\Delta t} \quad (9)$$

where E is the energy density (Wh kg^{-1}), C_s is the specific capacitance (F g^{-1}), V is the capacitor potential window excluding the IR drop (V), P is the power density (W kg^{-1}), and Δt is the discharge time (s).

3. Results and Discussion

The compositions of the synthesized $(\text{NH}_4)_2\text{MoS}_4$ and NiMoS_4 were examined by X-ray Diffraction (XRD). As shown in Figure 1a, the diffraction peaks of the as-prepared $(\text{NH}_4)_2\text{MoS}_4$ matched well with the orthorhombic $(\text{NH}_4)_2\text{MoS}_4$ (ICCD 00-048-1662), specifically, the major peaks at around 14.6° , 17.3° , 18.5° , 29.1° and 37.5° can be indexed to the crystal planes (011) (111) (200) (040) and (400) respectively. These results indicate that the $(\text{NH}_4)_2\text{MoS}_4$ was successfully prepared. NiMoS_4 was obtained by reacting $(\text{NH}_4)_2\text{MoS}_4$ with nickel nitrate. No peaks were found on the XRD patterns of NiMoS_4 (Figure 1b), showing typical amorphous features, which is consistent with the results reported in the literature.²³ As the NiMoS_4 was further calcined at 450°C , obvious diffraction peaks appeared on the NiMoS_4 -A patterns (Figure 1b). The peaks at 14.2° , 33.0° and 58.4° could be assigned to the (003) (101) and (110) planes of MoS_2 (ICDD 04-008-2233) while the peaks at 31.4° , 35.3° , 38.8° , 45.1° , 53.4° and 60.9° corresponded to the (200) (210) (211) (220) (311) and (321) planes of NiS_2 (ICCD 04-003-1992). The results reveal that the NiMoS_4 -A sample contains small quantities of poorly crystalized NiS_2 and MoS_2 .

To investigate morphology properties of the synthesized materials, scanning electron microscopy (SEM) was carried out for NiMoS_4 and NiMoS_4 -A. As shown in Figure 2a and b,

NiMoS₄ is composed of irregular particles. For NiMoS₄-A (Figure 2c and d), the particles are loosely agglomerated forming porous structures, which could improve the access of the electrolyte into the material during charge-discharge, thus promoting energy storage performances. Energy-dispersive X-ray spectroscopy studies (EDX) were conducted to determine the element compositions in the samples. Elements Ni, Mo, and S are observed in NiMoS₄ according to the EDX spectrum (Figure 3a), which is in agreement with the reagents used during the preparation processes. The distribution of each element was identified through elemental mapping as shown in Figure 3b. Clearly, the Ni, Mo, and S elements are uniformly distributed, the same result was also found for the NiMoS₄-A sample (Figure S1), indicating that possible agglomeration of the segregated NiS₂ and MoS₂ is not significant.

The prepared electrodes were examined in a three-electrode system using a 2M KOH electrolyte in order to explore the electrochemical properties. Figure 4a indicates the cyclic voltammetry (CV) curves of NiMoS₄ at different scan rate from 1 to 20 mV s⁻¹ in a potential window of 0 to 0.5 V vs. Ag/AgCl. Redox peaks are found in the CV curves, demonstrating that the energy storage ability is mainly contributed by the Faradaic redox reactions. It can be clearly seen that the CV curves exhibit a similar shape over all the scans, indicating good kinetic reversibility of the NiMoS₄ electrode.^{33, 34} Moreover, it can be deduced that the electrode presents low polarization³³ and rapid electronic and ionic transportation^{18,35} since the anodic and cathodic peaks slightly shift towards the positive and negative potentials respectively at increasing scan rates. The CV curves of NiMoS₄-A at different scan rates are presented in Figure 4b. It is evident that CV behaviors similar to that of NiMoS₄ were observed. However, sample NiMoS₄-A exhibits larger current density responses than NiMoS₄ at same scan rate. Figure 4c displays the CV plots of NiMoS₄ and NiMoS₄-A at 10 mV s⁻¹, it is believed that the integral area of CV curves is proportional to the specific capacity.³⁶ Obviously, the CV curves of NiMoS₄-A enclose a larger area than that of NiMoS₄, suggesting that a larger number

charges can be stored in the NiMoS₄-A electrode. The specific capacities of NiMoS₄ and NiMoS₄-A calculated based on the corresponding CV curves at different scan rates are shown in Figure 4d. The specific capacity of NiMoS₄-A is 353.4 C g⁻¹ at 1 mV s⁻¹, larger than the value for NiMoS₄ (286.8 C g⁻¹). All the capacities experience gradual decrease with increasing scan rate, reaching 231.5 C g⁻¹ and 166.2 C g⁻¹ at 20 mV s⁻¹ for NiMoS₄-A and NiMoS₄ respectively. It can be seen that the NiMoS₄-A performs better in terms of rate capability than NiMoS₄, namely, retaining 65.5% vs. 57.9% from 1 to 20 mV s⁻¹.

Galvanostatic charge–discharge (GCD) measurements for NiMoS₄ and NiMoS₄-A with current densities ranging from 1 to 10 A g⁻¹ are recorded in Figure 5a and b respectively. It can be seen that both NiMoS₄ and NiMoS₄-A exhibit nonlinear charge–discharge GCD curves, which further support the Faradaic behaviors of these materials. Figure 5d compares GCD curves of NiMoS₄ and NiMoS₄-A at a current density of 1 A g⁻¹. It shows that more charge can be stored on the NiMoS₄-A electrode due to its longer discharge time, which is consistent with the above CV results. The specific capacities calculated based on the GCD curves are shown in Figure 5d. NiMoS₄-A exhibits a good specific capacity of 313 C g⁻¹ at a current density of 1 A g⁻¹. At current densities of 2, 4, 6, 8, and 10 A g⁻¹, the specific capacities are 295, 274.4, 265.2, 256, and 248 C g⁻¹ respectively. This means that roughly 83% of the capacity can be maintained with a 10-fold increase in the current density, implying an excellent rate capability of the NiMoS₄-A sample. The gradual decrease in specific capacity could be ascribed to insufficient active materials involved in the redox reaction as diffusion time is limited for electrolyte ions accessing the active materials at high charge-discharge rates.³⁷ Noticeably, sample NiMoS₄-A has a superior specific capacity to that of sample NiMoS₄, specifically, only 221 C g⁻¹ is achieved by NiMoS₄ at 1 A g⁻¹ and 67% of the initial value is preserved when the current increases to 10 A g⁻¹.

The differences of electrochemical performance between samples NiMoS₄ and NiMoS₄-A are partially related to the impedance of the electrode. Therefore, electrochemical impedance spectroscopy (EIS) was carried out to further explore charge-transfer kinetics. Figure 5e depicts the Nyquist plots of NiMoS₄ and NiMoS₄-A at open circuit potential. It is evident that the graph is composed of a semicircle in high frequency region and a linear part in low frequency region. An equivalent circuit for fitting the Nyquist plots is shown in Figure 5f,^{38, 39} where R_s is the internal resistance, which is also known as equivalent series resistance (ESR), R_{ct} is the charge transfer resistance, W_0 is the Warburg impedance, C_{dl} is the electric double layer capacity, C_p is the faradaic capacity, and R_L is the leakage resistance. The fitting curve and the experimental data match very well with each other (Figure S2), confirming that the proposed equivalent circuit model is suitable for the electrode. The internal resistance (R_s), containing the bulk resistance of the electrolyte, the intrinsic resistance of the active materials and the contact resistance from the interface of active material and current collector,^{18, 40} could be estimated by the intersection of the curves on the real axis. The R_s for NiMoS₄-A is 0.53 Ω , slightly lower than 0.62 Ω for NiMoS₄, suggesting that the NiMoS₄-A possesses higher conductivity. The R_{ct} , demonstrating the rate of Faradaic redox process at the electrode-electrolyte interface,³⁸ can be evaluated by the diameter of the semicircle. Sample NiMoS₄-A exhibits smaller R_{ct} (1.9 Ω) than that for sample NiMoS₄ (3.2 Ω), implying the faster electron transfer on the NiMoS₄-A electrode, possibly owing to the porous morphology of NiMoS₄-A, which could facilitate the diffusion of electrolyte into the active materials, thus lowering the charge resistance. The straight line at low frequencies is associated with the Warburg impedance (W_0), which is supposed to describe the diffusive resistance of electrolyte ions within the electrode.⁴¹ Sample NiMoS₄-A exhibits a more vertical line, showing lower mass-transfer resistance in the host materials. Overall, the better impedance performances in terms of R_s , R_{ct} and W_0 for NiMoS₄-

A should lead to improved electrochemical properties, which has been confirmed by the previous CV and GCD results.

Normally, the total charge stored in the electrode is contributed by two different processes: the surface capacitive process and the diffusion controlled Faradaic effect. CV data could provide the insight into the charge storage mechanism based on the following equation:^{42, 43}

$$i = av^b \quad (9)$$

Where i is the measured current response, v is the scan rate, and a and b are adjustable parameters. In the condition of $b = 1$, the current indicates the surface capacitive component, while when $b = 0.5$, the current represents the diffusion controlled Faradaic component. Therefore, the total current at a fixed potential can be expressed as:^{42, 44}

$$i = k_1v + k_2v^{1/2} \quad (10)$$

where k_1v and $k_2v^{1/2}$ correspond to the current contribution by surface capacitive process and the diffusion controlled Faradaic effect, respectively. For analytical purpose, we rearrange the equation to

$$i/v^{1/2} = k_1v^{1/2} + k_2 \quad (11)$$

By plotting the $i/v^{1/2}$ vs. $v^{1/2}$ at different potentials, the values of k_1 (slope) and k_2 (intercept) could be determined, thus the specific current contribution at each potential could be obtained. Finally, the fraction of the charge stored from capacitive effect and diffusion-controlled Faradaic process could be extracted quantitatively by integrating the CV area. In Figure 6a, the current response of diffusion controlled process (blue area) on the NiMoS₄-A electrode is compared with total current at a scan rate of 5 mV s⁻¹. The diffusion controlled process occupies around 61% of the total charge storage and the remaining portion is originated from the surface capacitive effect. Based on the same approach, the percentages of diffusion controlled process on NiMoS₄ and NiMoS₄-A electrodes at various scan rate are compared in Figure 6b. The two materials present quite similar trends, namely, the diffusion controlled process contribution

gradually decreases with increase in scan rate, reaching around 40% at a scan rate of 20 mV s⁻¹. In other words, the Faradaic redox process dominates at lower scan rates while the capacitive effect matters at higher scan rates. However, at each specific scan rate, the percentage of diffusion controlled process is slightly higher on the sample NiMoS₄-A than that on the sample NiMoS₄, suggesting easier redox reactions on the NiMoS₄-A electrode, which is well in accordance with the impedance results.

Clearly, as an energy storage material, the electrochemical performance of NiMoS₄-A is superior than that of NiMoS₄, which could be related to the heating process. XRD shows that weak peaks of NiS₂ and MoS₂ appear after heating in Ar. It is supposed that the interaction between the MoS₂ and NiS₂ components could promote the activity and improve its conductivity.²³ Our impedance results have also confirmed the lower resistance of NiMoS₄-A. Therefore, it can be concluded that the synergistic effect between the small amount of MoS₂ and NiS₂ in sample NiMoS₄-A improves the electrochemical performance of the electrode, resulting in a higher specific capacity of the NiMoS₄-A than that of the NiMoS₄.

To further explore the electrochemical properties of the NiMoS₄-A electrode in a practical energy storage device, a hybrid supercapacitor (HSC) was fabricated using NiMoS₄-A as the positive electrode and activated carbon (AC) as the negative electrode. The AC electrode performs a typical feature of EDLC (Figure S3). Figure 7a demonstrates the CV curves of NiMoS₄-A//AC HSC with different voltages ranging from 1.0 to 1.7 V at a scan rate of 5 mV s⁻¹. Obviously, the HSC has a stable performance with voltages up to 1.6 V, however when the voltage extends to 1.7 V a polarization curve appears with a much higher current response, suggesting that a severe side reaction of water electrolysis is taking place. Consequently, the operating voltage window for the HSC is selected as 0 to 1.6 V. The CV curves of the HSC at various scan rates are shown in Figure 7b. The quasi-rectangular CV shape at all scans reveals that the energy stored in this HSC originates from hybrid effects of the electric double-layer

and Faradaic redox effects, this is further confirmed by the GCD curves (Figure 7c). The lower the current densities, the more obviously non-linear the charge-discharge curves are. The specific capacitances of the HSC based on Equation 7 are calculated in Figure 7d. There is a significant decrease from 0.5 to 2 A g⁻¹, but from 2 to 20 A g⁻¹, the values remains stable, indicating a good rate capability. Specifically, 101.3, 84.6, 73.1, 67.1, 63.8, 60.5, and 59.1 F g⁻¹ are achieved at current density of 0.5, 1, 2, 5, 10, 15, and 20 A g⁻¹ respectively (Figure 7d), higher than those of other similar HSCs, such as CoMoS₄/rGO (77 F g⁻¹ at 0.5 A g⁻¹)⁴⁵ and NiMoO₄-rGO//N-doped graphene (84 F g⁻¹ at 0.5 A g⁻¹)³⁶. The durability of the HSC was evaluated over 10000 cycles at a current density of 5 A g⁻¹ (Figure 7e). As seen from the graph, about 8% of the initial capacitance is lost during the first 200 cycles, after that, the value remains almost constant, showing an overall capacitance retention of 82% after 10000 cycles. The impedance spectra before and after the cyclic test is shown in the inset of Figure 7e. The R_s is nearly unchanged and the R_{ct} increases by about only 0.6 Ω after the 10000 cycle test, confirming the outstanding stability. The first and last ten cycles of the GCD curves are presented in Figure S4. The excellent electrochemical stability could be attributed to the structural features of the materials. In particular, the effective interfacial area between the active materials and the electrolyte could facilitate the electrolyte accessing the active sites. Moreover, the porous structure could buffer the volume change during rapid charge-discharge process and prevent structural collapse.

Specific energy and power densities are two key parameters to investigate in an electrochemical energy storage device.¹⁹ The Ragone plots of the HSC are displayed in Figure 7f. The obtainable highest energy density is 35 Wh kg⁻¹ at a power density of 400 W kg⁻¹, which is comparable to those of previously reported devices, such as Co₉S₈ nanoflakes//AC (31.4 Wh kg⁻¹ at 200 W kg⁻¹)⁴¹, CoMoS₄/rGO (27.2 Wh kg⁻¹ at 400 W kg⁻¹)⁴⁵ and CoMoO₄-graphene//AC (21.1 Wh kg⁻¹ at 300 W kg⁻¹)⁴⁶. The high energy density should benefit from the

high capacitance of NiMoS₄-A electrode. The HSC still delivers an energy density of 13.5 Wh kg⁻¹ at a very high power density around 13000 W kg⁻¹.

4. Conclusion

We have synthesized NiMoS₄-A through a facile chemical co-precipitation process followed by calcining at 450 °C. The NiMoS₄-A electrode performs with a good specific capacity of 313 C g⁻¹ at 1 A g⁻¹ while still maintaining 83% at 10 A g⁻¹ in a KOH electrolyte. The detailed charge storage mechanism analysis reveals that surface capacitive process and diffusion controlled Faradaic reaction contribute together to the energy storage, and that the Faradaic redox process dominates at lower scan rates (78% at 1 mV s⁻¹) while the capacitive effect matters at higher scan rate (56% 20 mV s⁻¹). Furthermore, a hybrid supercapacitor (HSC) was fabricated using NiMoS₄-A as the positive electrode and activated carbon (AC) as the negative electrode. The HSC delivers 1.6 V cell voltage and 35 Wh kg⁻¹ energy density at a power density of 400 W kg⁻¹. Additionally, the HSC exhibits good cycle stability, retaining 82% of the initial capacitance after 10000 charge-discharge cycles even at a high current density of 5 A g⁻¹. These good electrochemical performances indicate the great potential of NiMoS₄-A for hybrid supercapacitors.

Acknowledgements

One of the authors (Du) thanks University of Warwick for a PhD studentship.

Supporting Information

Supporting Information is available online.

References

1. G. Yu, X. Xie, L. Pan, Z. Bao, and Y. Cui, *Nano Energy*, **2** (2), 213-234 (2013).
2. V. Etacheri, R. Marom, R. Elazari, G. Salitra, and D. Aurbach, *Energy Environ. Sci.*, **4** (9), 3243-3262 (2011).
3. M. Armand and J.-M. Tarascon, *Nature*, **451** (7179), 652-657 (2008).
4. S. Faraji and F. N. Ani, *Renewable Sustainable Energy Rev.*, **42** 823-834 (2015).
5. M. Winter and R. J. Brodd. ACS Publications, 2004.
6. P. Simon and Y. Gogotsi, *Nat. Mater.*, **7** (11), 845-854 (2008).
7. G. Wang, L. Zhang, and J. Zhang, *Chem. Soc. Rev.*, **41** (2), 797-828 (2012).
8. Y. Wang, Y. Song, and Y. Xia, *Chem. Soc. Rev.*, **45** (21), 5925-5950 (2016).
9. S. Vijayakumar, S. Nagamuthu, and G. Muralidharan, *ACS Appl. Mater. Interfaces*, **5** (6), 2188-2196 (2013).
10. H. Chen, L. Hu, M. Chen, Y. Yan, and L. Wu, *Adv. Funct. Mater.*, **24** (7), 934-942 (2014).
11. H. Hu, B. Y. Guan, and X. W. D. Lou, *Chem*, **1** (1), 102-113 (2016).
12. C. Choi, H. J. Sim, G. M. Spinks, X. Lepró, R. H. Baughman, and S. J. Kim, *Adv. Energy Mater.*, (2016).
13. Z. Ye, B. Wang, G. Liu, Y. Dong, X. Cui, X. Peng, A. Zou, and D. Li, *J. Electrochem. Soc.*, **163** (13), A2725-A2732 (2016).
14. G. Meng, Q. Yang, X. Wu, P. Wan, Y. Li, X. Lei, X. Sun, and J. Liu, *Nano Energy*, **30** 831-839 (2016).
15. V. Kannan, A. I. Inamdar, S. M. Pawar, H.-S. Kim, H.-C. Park, H. Kim, H. Im, and Y. S. Chae, *ACS Appl. Mater. Interfaces*, **8** (27), 17220-17225 (2016).
16. H.-S. Kim, J. B. Cook, H. Lin, J. S. Ko, S. H. Tolbert, V. Ozolins, and B. Dunn, *Nat. Mater.*, **16** (4), 454-460 (2017).
17. T. Brezesinski, J. Wang, S. H. Tolbert, and B. Dunn, *Nat. Mater.*, **9** (2), 146-151 (2010).
18. M. Guo, J. Balamurugan, T. D. Thanh, N. H. Kim, and J. H. Lee, *J. Mater. Chem. A*, **4** (44), 17560-17571 (2016).
19. H. Pang, C. Wei, X. Li, G. Li, Y. Ma, S. Li, J. Chen, and J. Zhang, *Sci Rep*, **4** 3577 (2014).
20. M. Acerce, D. Voiry, and M. Chhowalla, *Nat. Nanotechnol.*, **10** (4), 313-318 (2015).
21. D. Guo, P. Zhang, H. Zhang, X. Yu, J. Zhu, Q. Li, and T. Wang, *J. Mater. Chem. A*, **1** (32), 9024-9027 (2013).
22. S. Peng, L. Li, H. B. Wu, S. Madhavi, and X. W. D. Lou, *Adv. Energy Mater.*, **5** (2), (2015).
23. L. Shao, X. Qian, X. Wang, H. Li, R. Yan, and L. Hou, *Electrochim. Acta*, **213** 236-243 (2016).
24. X. Zheng, J. Guo, Y. Shi, F. Xiong, W.-H. Zhang, T. Ma, and C. Li, *Chem. Commun.*, **49** (83), 9645-9647 (2013).
25. Y.-H. Dai, L.-B. Kong, K. Yan, M. Shi, T. Zhang, Y.-C. Luo, and L. Kang, *RSC Adv.*, **6** (9), 7633-7642 (2016).
26. Z. Fan, J. Yan, T. Wei, L. Zhi, G. Ning, T. Li, and F. Wei, *Adv. Funct. Mater.*, **21** (12), 2366-2375 (2011).
27. R. Li, Y. Wang, C. Zhou, C. Wang, X. Ba, Y. Li, X. Huang, and J. Liu, *Adv. Funct. Mater.*, **25** (33), 5384-5394 (2015).
28. J. Yang, X. Duan, W. Guo, D. Li, H. Zhang, and W. Zheng, *Nano Energy*, **5** 74-81 (2014).

29. X. Wang, A. Sumboja, M. Lin, J. Yan, and P. S. Lee, *Nanoscale*, **4** (22), 7266-7272 (2012).
30. D. Du, R. Lan, K. Xie, H. Wang, and S. Tao, *RSC Adv.*, **7** (22), 13304-13311 (2017).
31. V. Khomenko, E. Raymundo-Pinero, and F. Béguin, *J. Power Sources*, **153** (1), 183-190 (2006).
32. D. Du, R. Lan, W. Xu, R. Beanland, H. Wang, and S. Tao, *J. Mater. Chem. A*, **4** (45), 17749-17756 (2016).
33. Y. Lei, J. Li, Y. Wang, L. Gu, Y. Chang, H. Yuan, and D. Xiao, *ACS Appl. Mater. Interfaces*, **6** (3), 1773-1780 (2014).
34. S. E. Moosavifard, J. Shamsi, S. Fani, and S. Kadkhodazade, *RSC Adv.*, **4** (94), 52555-52561 (2014).
35. Y. Cao, W. Li, K. Xu, Y. Zhang, T. Ji, R. Zou, J. Yang, Z. Qin, and J. Hu, *J. Mater. Chem. A*, **2** (48), 20723-20728 (2014).
36. T. Liu, H. Chai, D. Jia, Y. Su, T. Wang, and W. Zhou, *Electrochim. Acta*, **180** 998-1006 (2015).
37. J.-G. Wang, Y. Yang, Z.-H. Huang, and F. Kang, *J. Mater. Chem.*, **22** (33), 16943-16949 (2012).
38. W. Wang, S. Guo, I. Lee, K. Ahmed, J. Zhong, Z. Favors, F. Zaera, M. Ozkan, and C. S. Ozkan, *Sci. Rep.*, **4** 4452 (2014).
39. Z. Niu, W. Zhou, J. Chen, G. Feng, H. Li, W. Ma, J. Li, H. Dong, Y. Ren, and D. Zhao, *Energy Environ. Sci.*, **4** (4), 1440-1446 (2011).
40. S. Khalid, C. Cao, A. Ahmad, L. Wang, M. Tanveer, I. Aslam, M. Tahir, F. Idrees, and Y. Zhu, *RSC Adv.*, **5** (42), 33146-33154 (2015).
41. R. Rakhi, N. A. Alhebshi, D. H. Anjum, and H. N. Alshareef, *J. Mater. Chem. A*, **2** (38), 16190-16198 (2014).
42. X. Zhang, J. Luo, P. Tang, X. Ye, X. Peng, H. Tang, S.-G. Sun, and J. Fransaer, *Nano Energy*, **31** 311-321 (2017).
43. V. Augustyn, J. Come, M. A. Lowe, J. W. Kim, P.-L. Taberna, S. H. Tolbert, H. D. Abruña, P. Simon, and B. Dunn, *Nat. Mater.*, **12** (6), 518-522 (2013).
44. X. Xia, D. Chao, Y. Zhang, J. Zhan, Y. Zhong, X. Wang, Y. Wang, Z. X. Shen, J. Tu, and H. J. Fan, *Small*, **12** (22), 3048-3058 (2016).
45. X. Xu, Y. Song, R. Xue, J. Zhou, J. Gao, and F. Xing, *Chem. Eng. J.*, **301** 266-275 (2016).
46. X. Yu, B. Lu, and Z. Xu, *Adv. Mater.*, **26** (7), 1044-1051 (2014).

List of Figures

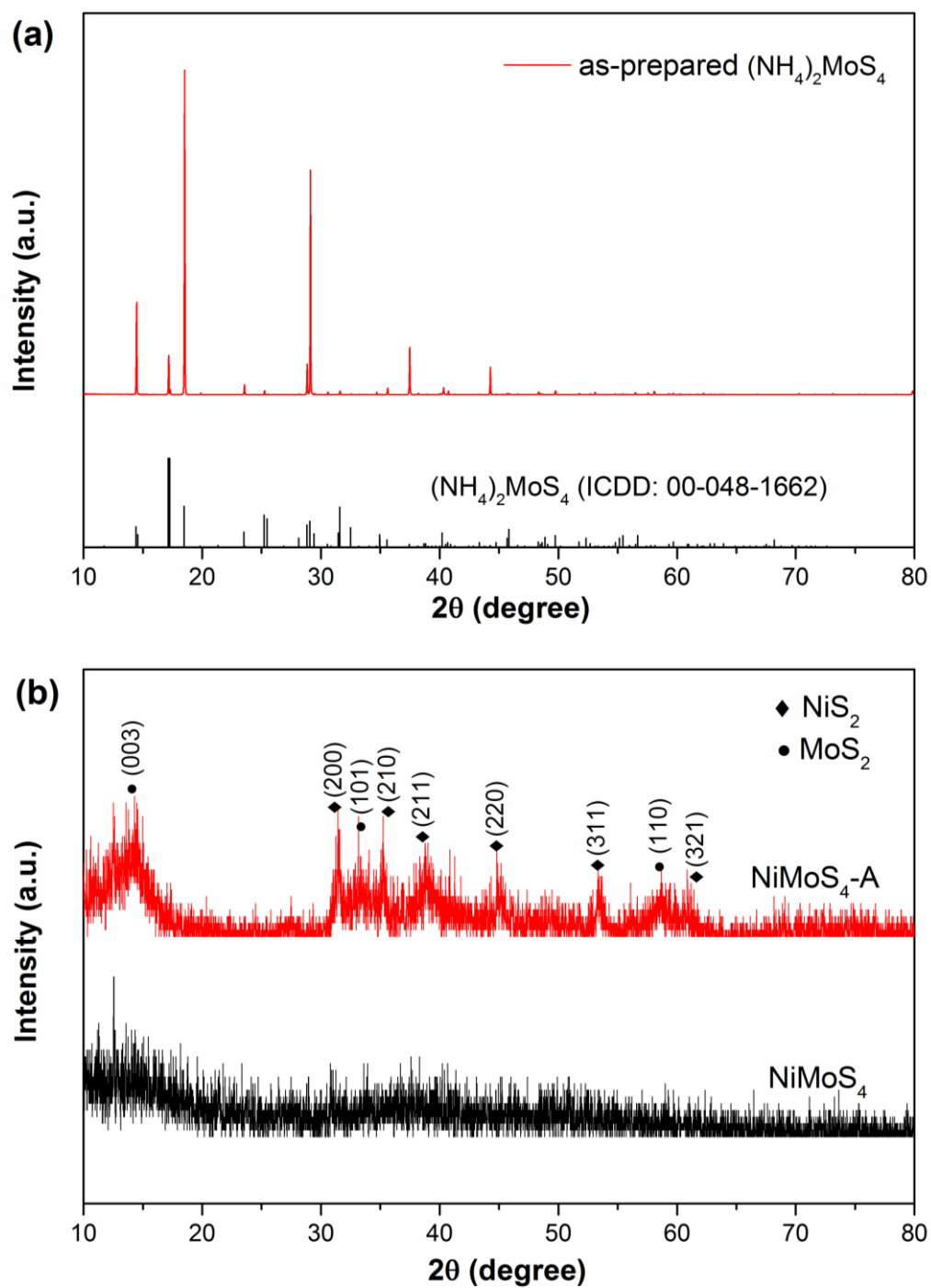


Figure 1. XRD patterns of (a) $(\text{NH}_4)_2\text{MoS}_4$, (b) NiMoS_4 and $\text{NiMoS}_4\text{-A}$.

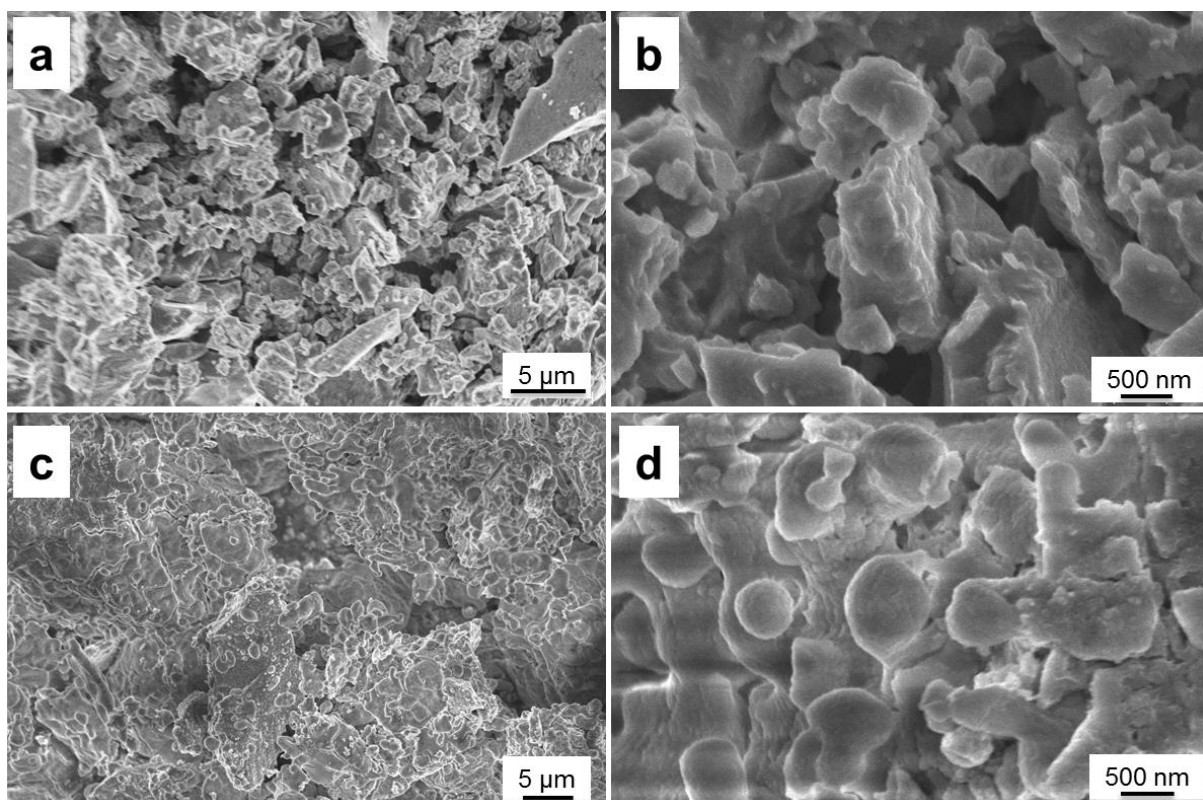


Figure 2. SEM images of (a-b) NiMoS_4 and (c-d) $\text{NiMoS}_4\text{-A}$.

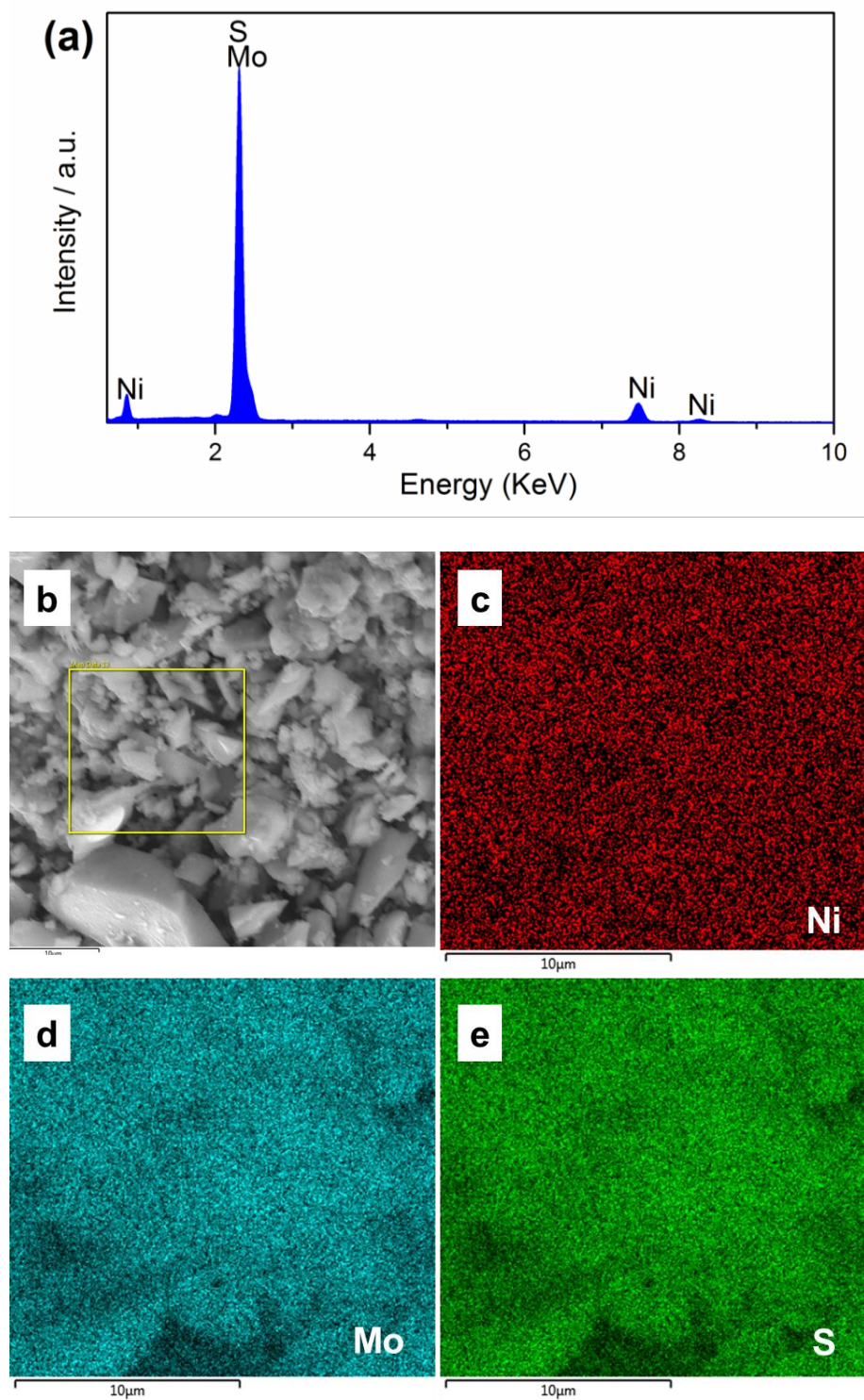


Figure 3. (a) EDX spectrum and (b-f) elemental mapping of NiMoS_4 .

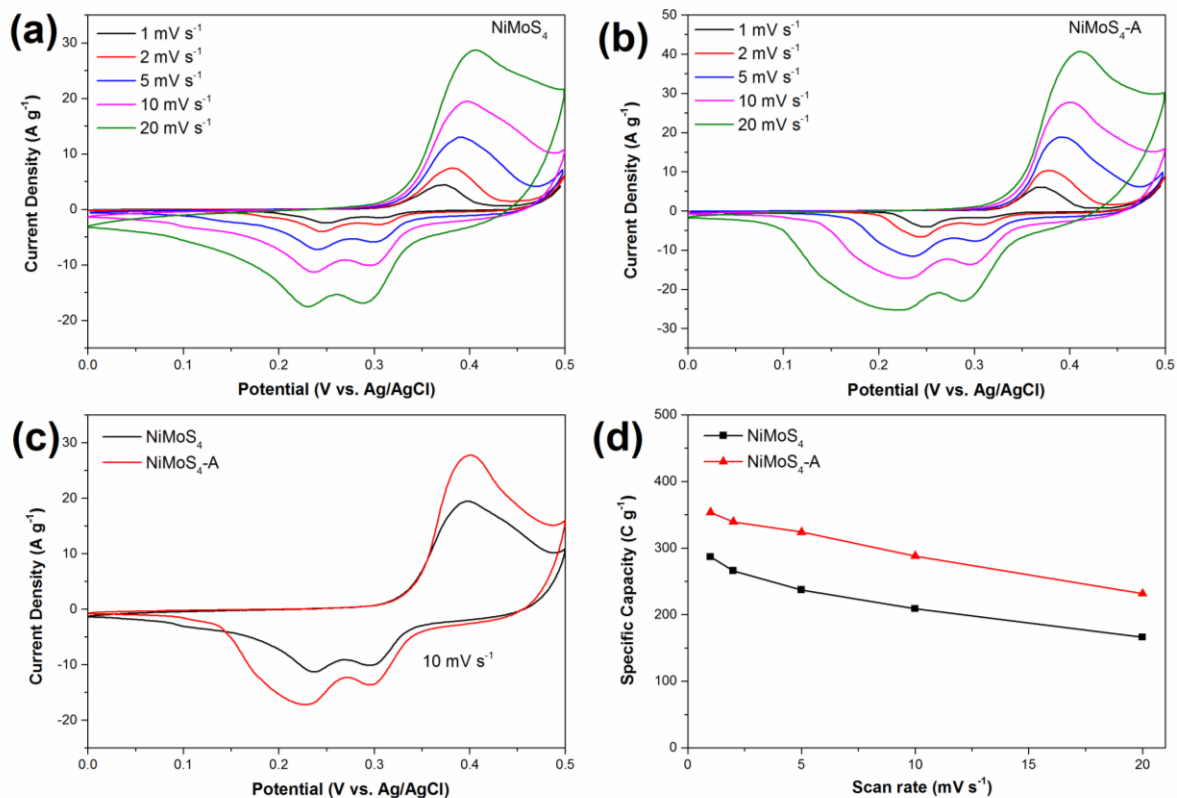


Figure 4. CV curves at different scan rates of (a) NiMoS_4 and (b) $\text{NiMoS}_4\text{-A}$. (c) Comparison of CV curves of NiMoS_4 and $\text{NiMoS}_4\text{-A}$ electrode at scan rate of 10 mV s^{-1} . (d) Specific capacities at various scan rates.

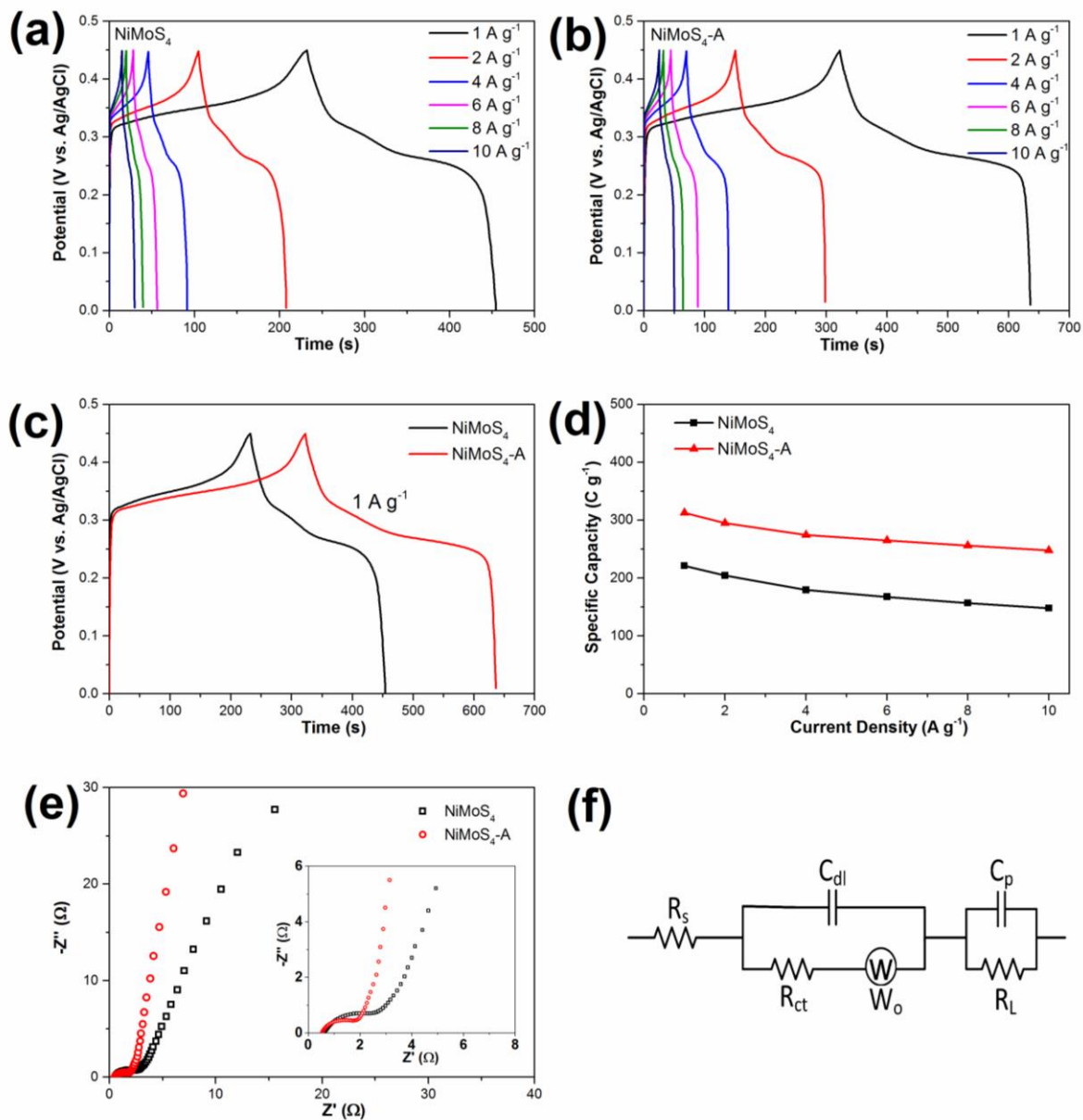


Figure 5. GCD curves at different current density of (a) NiMoS_4 and (b) $\text{NiMoS}_4\text{-A}$. (c) Comparison of GCD curves of NiMoS_4 and $\text{NiMoS}_4\text{-A}$ electrode at current density of 1 A g^{-1} . (d) Specific capacities at various current densities. (e) Nyquist plots at open circuit potential. (f) The equivalent circuit.

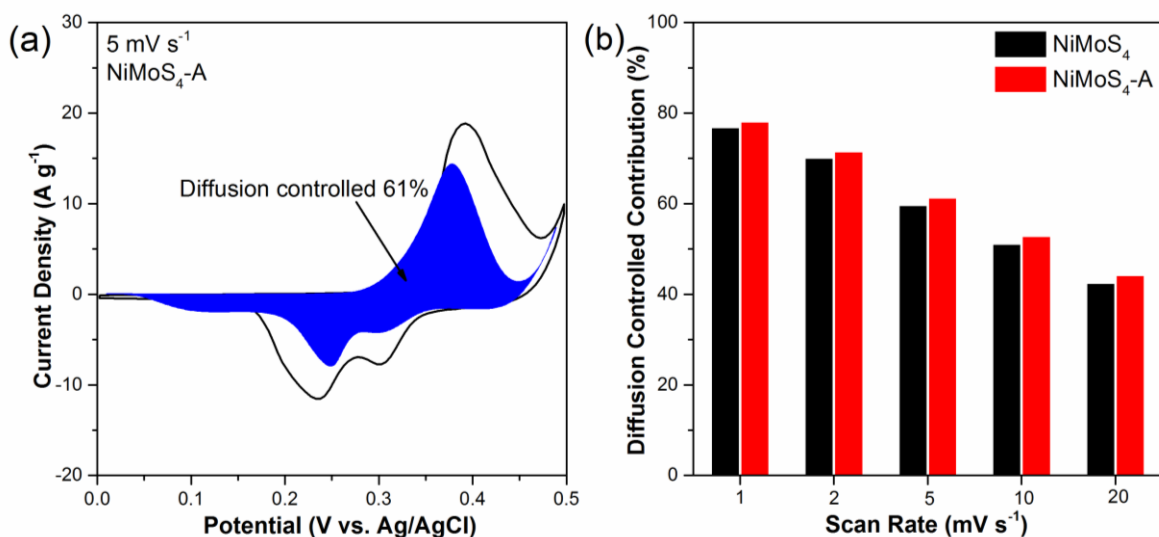


Figure 6. a) Typical separation of capacitive and diffusion-controlled charge storage process at scan rate of 5 mV s⁻¹ of NiMoS₄-A, b) Faradaic diffusion-controlled process contribution to the total charge stored at various scan rate in NiMoS₄ and NiMoS₄-A.

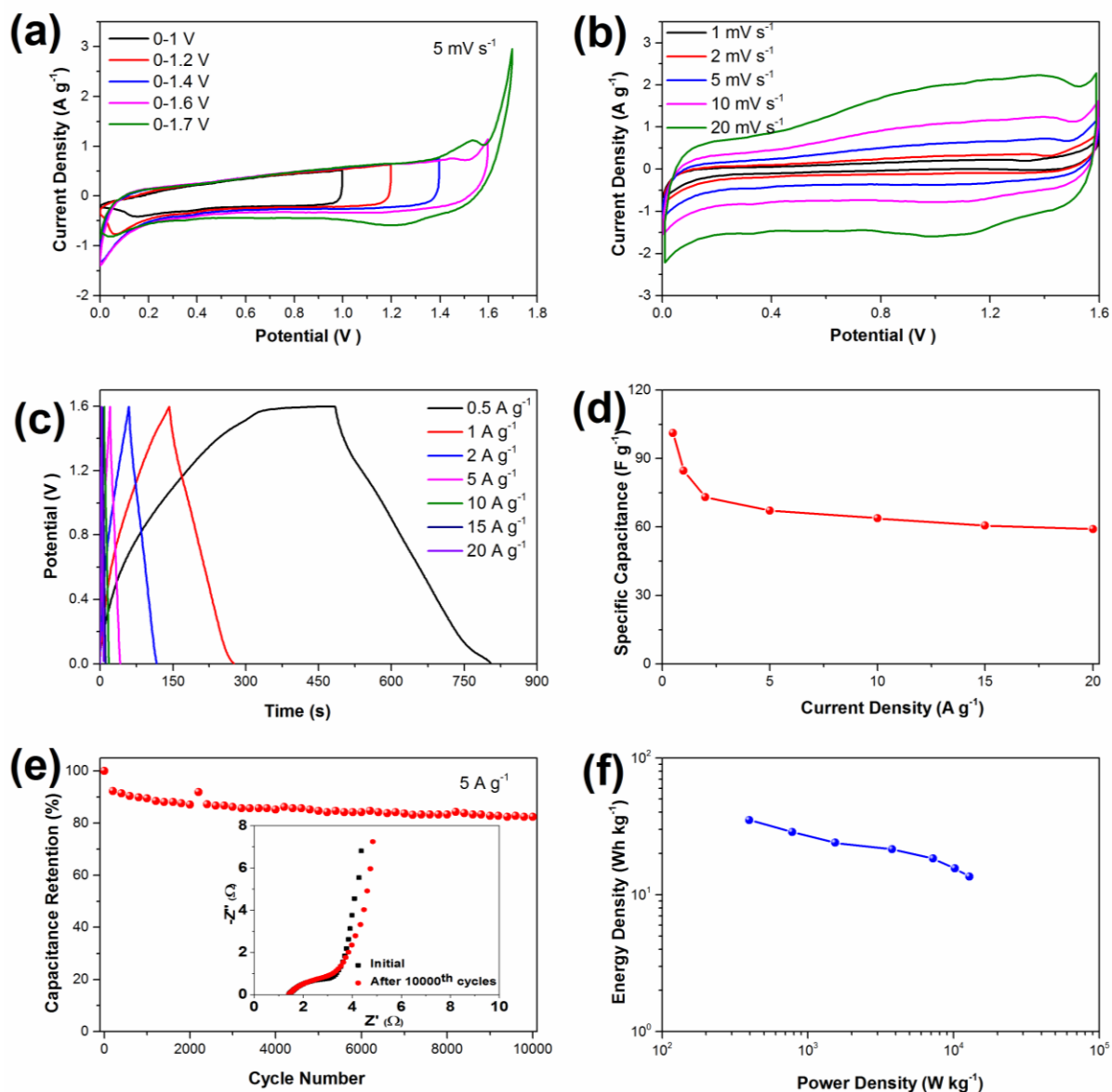


Figure 7. Electrochemical properties of NiMoS₄-A//AC hybrid supercapacitor: a) CV curves at various voltage windows at 5 mV s⁻¹; b) CV curves with a voltage window of 0-1.6 V at various scan rate; c) Galvanostatic charge-discharge curves at various current densities; d) Specific capacitance at various current densities. e) Cycling performances of the hybrid supercapacitor for 10000 cycles at 5 A g⁻¹; f) Ragone plots of the supercapacitor based on total mass of active materials.

Supporting Materials for

Synthesis of NiMoS₄ for high-performance hybrid supercapacitors

Dongwei Du,^a Rong Lan,^a John Humphreys,^a Wei Xu,^a Kui Xie,^c Huanting Wang,^b and
Shanwen Tao,^{a,b,z}

^a School of Engineering, University of Warwick, Coventry CV4 7AL, UK

^b Department of Chemical Engineering, Monash University, Clayton, Victoria 3800, Australia

^c Key Lab of Design and Assembly of Functional Nanostructure, Fujian Institute of Research
on the Structure of Matter, Chinese Academy of Sciences, Fuzhou, Fujian 350002, China

^z Corresponding author: Shanwen Tao

E-mail: S.Tao.1@warwick.ac.uk

Tel: +44 (0)24 761 51680

Fax: +44 (0)24 76 418922

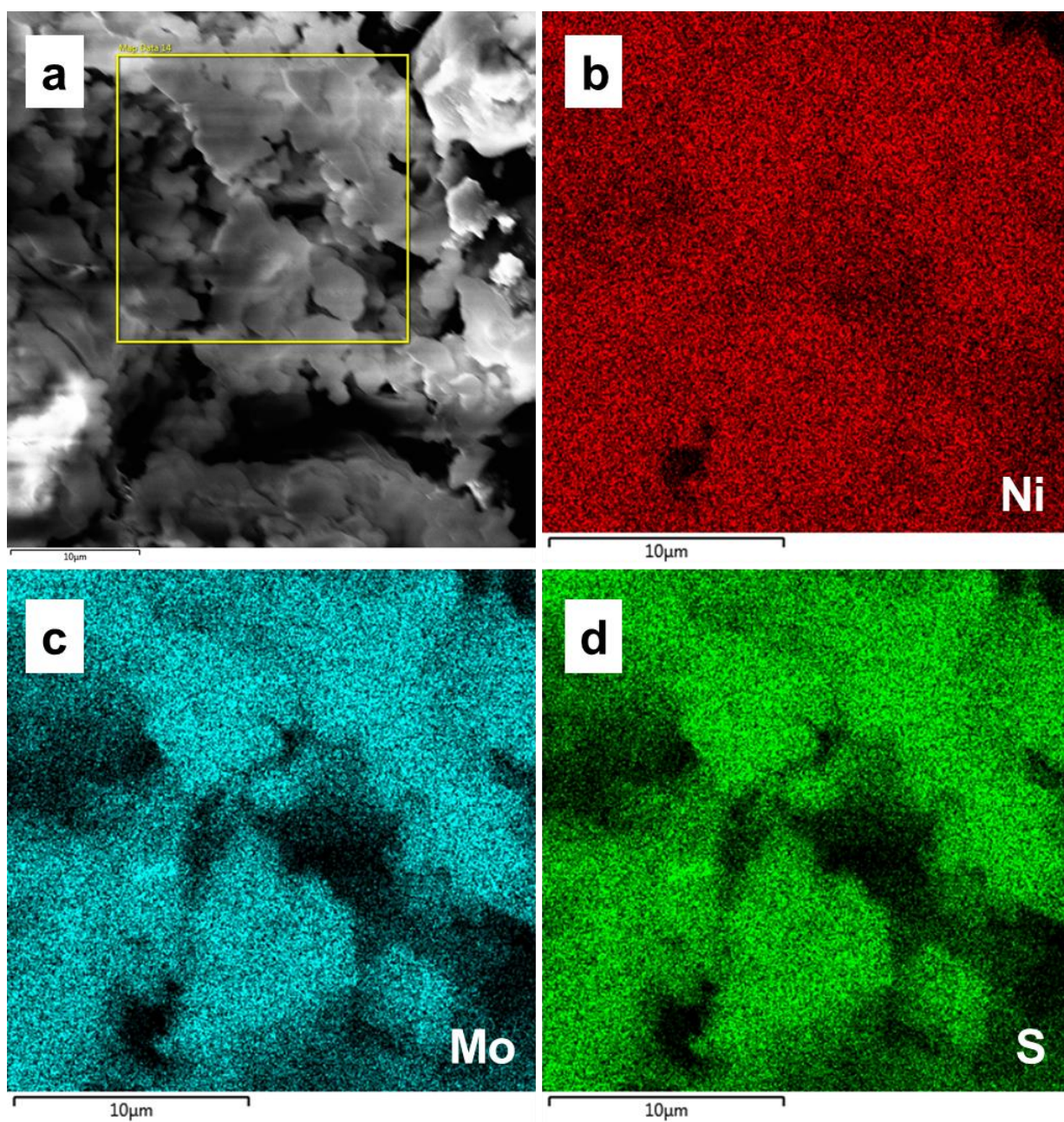


Figure S1. Elemental mapping of sample $\text{NiMoS}_4\text{-A}$.

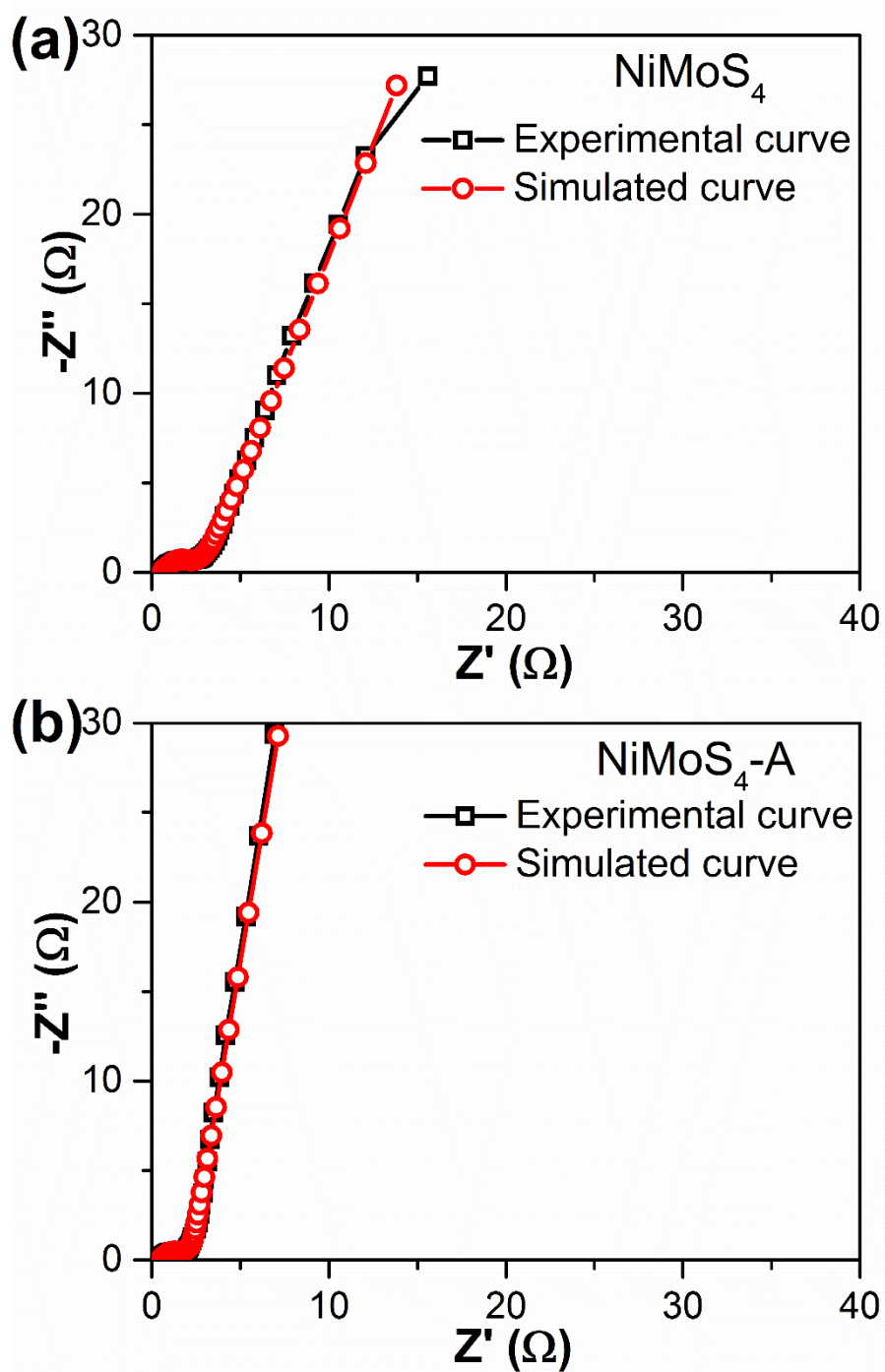


Figure S2. Experimental and simulated Nyquist plots of (a) NiMoS_4 and (b) $\text{NiMoS}_4\text{-A}$.

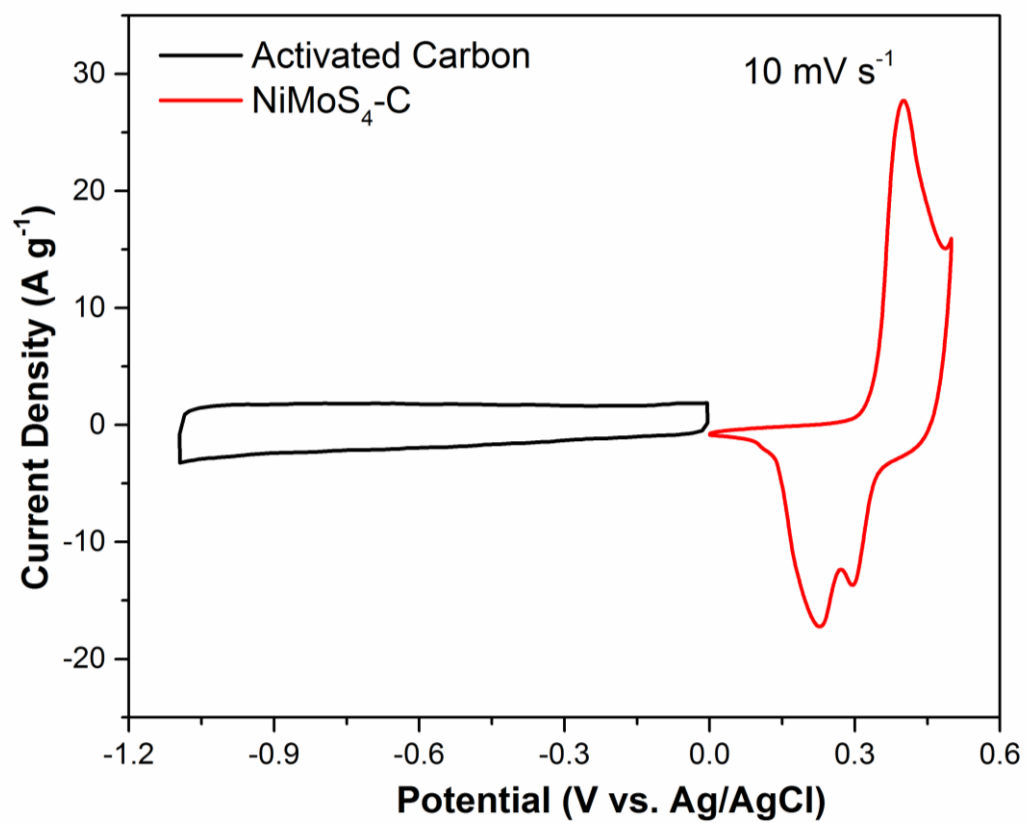


Figure S3. Comparative CV curves of activated carbon and NiMoS₄-A electrodes performed in 2 M KOH at a scan rate of 10 mV s^{-1} .

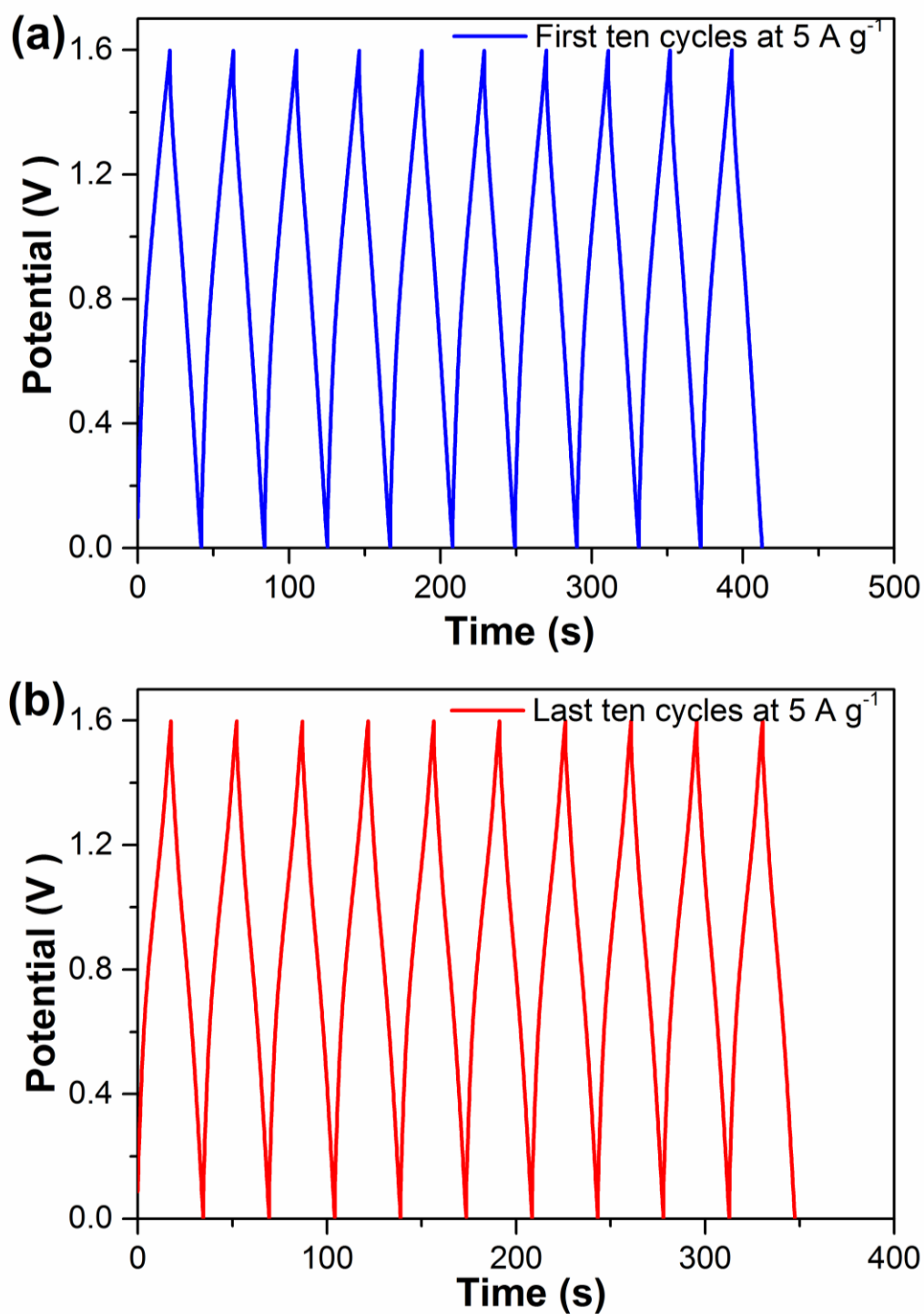


Figure S4. a) First and b) last ten charge-discharge curves of the NiMoS₄-A//AC hybrid supercapacitor at a current density of 5 A g⁻¹.